# Biomimetic 3D-printed gyroid scaffolds with versatile bioactive coatings for complex craniomaxillofacial bone regeneration

Biomedical Materials



OPEN ACCESS

RECEIVED
4 November 2025

REVISED
13 February 2026

ACCEPTED FOR PUBLICATION
23 March 2026

PUBLISHED
28 April 2026



PAPER

# Biomimetic 3D-printed gyroid scaffolds with versatile bioactive coatings for complex craniomaxillofacial bone regeneration

**Céline Tourbier**[1,2,5], **Valentina Basoli**[1,2,5,*], **Michaela Maintz**[1,2,3], **Elena Della Bella**[4], **Martin James Stoddart**[4] **and Florian M Thieringer**[1,2]

[1] Clinic of Oral and Cranio-Maxillofacial Surgery, University Hospital Basel, Spitalstr. 21, 4031 Basel, Switzerland
[2] Medical Additive Manufacturing Research Group (Swiss MAM) Department of Biomedical Engineering, University of Basel, Hegenheimermattweg 167B/C, 4123 Allschwil, Switzerland
[3] Institute for Medical Engineering and Medical Informatics IM[2] University of Applied Sciences and Arts Northwestern Switzerland, FHNW Hofackerstrasse 30, 4132 Muttenz, Switzerland
[4] AO Research Institute Davos, Clavadelerstrasse 8, 7270 Davos, Switzerland
[5] These authors have contributed equally to this work and share the first authorship.
[*] Author to whom any correspondence should be addressed.

**E-mail:** valentina.basoli@unibas.ch

**Keywords:** biomimetic scaffold, additive manufacturing, gyroid structure, mandibular bone regeneration, composite materials, bioactive coatings, multi-material printing

Supplementary material for this article is available online

## Abstract

Three-dimensional (3D) printing enables the fabrication of biomimetic scaffolds for craniomaxillofacial (CMF) bone regeneration, offering patient-specific solutions with tailored mechanical and biological properties. This study presents a 3D-printed gyroid scaffold composed of poly(L-lactide-co-D,L-lactide) (PLDLLA) and $\beta$-tricalcium phosphate ($\beta$-TCP), designed to enhance structural integrity and bioactivity. Using computer-aided design (CAD) and a dual-material additive manufacturing approach incorporating a water-soluble support material, scaffolds with controlled porosity and tunable mechanical properties are fabricated to match trabecular mandibular bone characteristics. Mechanical testing demonstrates that modulating wall thickness and porosity optimizes compressive strength and elastic modulus, ensuring stability under physiological loads. Chemical and cytotoxicity analyses confirm biocompatibility across manufacturing, post-processing, and sterilization. Biofunctionalization with polydopamine (PDA) and nano-hydroxyapatite (nHAP) enables selective cellular responses. PDA suppresses cell mineralization markers in osteosarcoma cells, while PDA-nHAP enhances osteogenic differentiation and fibroblast adhesion, supporting regenerative applications. High fidelity to CAD models and suitability for point-of-care fabrication underscore its clinical potential for CMF defect repair. By integrating tunable mechanics and targeted bioactivity, the developed scaffold offers a versatile platform for CMF reconstruction, addressing critical challenges in bone tissue engineering.

## Abbreviations

| | |
|---|---|
| 3D | Three-dimensional |
| AFJ | Arburg freeformer job |
| AM | Additive manufacturing |
| APF | Arburg plastic freeformer |
| BJ-1 | Human fibroblast cell line |
| CAD | Computer-aided design |
| CMF | Craniomaxillofacial |
| DMEM | Dulbecco's modified Eagle's medium |
| DMSO | Dimethyl sulfoxide |
| EDX | Energy-dispersive x-ray spectroscopy |
| FBS | Fetal bovine serum |
| FDM | Fused filament deposition |
| HAP | Hydroxyapatite |
| IBSP | Integrin-binding sialoprotein (bone sialoprotein |
| nHAP | Nano-hydroxyapatite |
| OCN | Osteocalcin |
| P | Porosity |

| | |
|---|---|
| PDA | Polydopamine |
| PLDLLA | Poly(L-lactide-co-D, L-lactide) |
| PEEK | Polyether ether ketone |
| PLA | Polylactic acid |
| POC | Point of care |
| RMS | Root mean square |
| SEM | Scanning electron microscopy |
| STL | Standard tessellation language |
| $\beta$-TCP | Beta tricalcium phosphate |
| TL | Transmitted light |
| TPMS | Triply periodic minimal surfaces |
| WT | Wall thickness |

## 1. Introduction

Bone defects in the CMF region often require grafts for repair. Limitations associated with the current gold standard, autologous bone grafting, such as high donor site morbidity and challenges in accurately shaping the graft to match craniofacial anatomy, have led to an interest in the use of synthetic scaffolds [1, 2].

Advances in computational design and AM have enabled the fabrication of 3D porous scaffolds and implants with precise architectures. 3D printing allows the production of constructs with a defined shape, size, porosity, and pore distribution, impacting mechanics, degradation, cell behavior, and tissue formation [3–5]. In addition, recent advances in 3D bioprinting have expanded the ability to generate biomimetic, spatially controlled 3D constructs, including organoid based systems [6]. It also offers to produce patient-specific designs, which are crucial in most CMF defects for functional and aesthetic restoration [7].

In our clinic, we have already embraced cutting-edge non-resorbable patient-specific cranial PEEK implants that are 3D printed at the POC [8]. These implants leverage medical imaging modalities like computer tomography and magnetic resonance imaging, along with CAD, ensuring precise replication of defects and providing effective solutions for cranial bone defects [9]. While these inert implants excel in addressing aesthetic concerns and protecting vital structures like the brain, there remains a challenge in fully restoring the integrity and function of the bone itself [10]. Identifying appropriate materials and workflows for resorbable 3D printing bone regeneration solutions poses a pivotal challenge, especially in achieving the necessary mechanical strength and biocompatibility for clinical application [11]. Optimal bone replacement scaffolds should closely mimic both the physical and chemical structure of natural bone, creating a conducive environment for cell growth [12]. Gyroid patterns are known for their uniformly distributed pores and struts, which help promote cell attachment and growth. They also provide good mechanical strength and stability, which is crucial for supporting bone tissue during regeneration [13–15]. Recent evidence suggests that TPMS, such as the gyroid, can drive the cell fate of human mesenchymal stromal cells towards osteogenic differentiation and enhance the cells' angiogenic paracrine function [16].

Extensive research has been conducted on synthetic polymers, including polylactic acid (PLA) and its derivatives, which are widely used in clinical applications due to their biocompatibility and biodegradability, especially in bone fixation and osteosynthesis plates [17]. With the development of 3D printing, research has progressed in tissue regeneration applications, including bone scaffolds [18]. However, the hydrophobic nature of these materials presents a challenge for cell adherence [19]. Indeed, many coatings have been employed to further enhance the performance of materials such as PLA-based scaffolds. Strategies such as fibrinogen coating have shown promise to overcome this limitation and allow for better cell adhesion [20]. However, the quest for clinically applicable solutions persists. In a previous study, we demonstrated that surface functionalization with polydopamine (PDA) and hydroxyapatite (HAP) resulted in improved hydrophilicity and controlled release of $Ca^{2+}$ to enhance cellular responses, including early osteogenic behavior [21]. PDA-coatings are versatile and widely studied materials in biomedical applications due to their strong adhesive properties and biocompatibility. Inspired by the natural adhesion mechanism of mussel foot proteins, PDA forms stable coatings on a wide range of surfaces, including metals, polymers, and ceramics, under mild conditions. These coatings offer functional groups, such as catechol and amine, which enable further functionalization and enhance the material's bioactivity [21]. PDA has been particularly effective in promoting mineralization by providing nucleation sites for HAP formation, making it valuable for bone regeneration applications [22]. These unique properties make PDA coatings highly suitable for multifunctional applications, such as combining bone regeneration with cancer therapy or enabling controlled drug delivery [21, 23, 24].

Clinical studies also support the use of beta-tricalcium phosphate ($\beta$-TCP) as a synthetic bone graft substitute [25] with good cell-mediated resorption as well as osteoconductive and osteoinductive properties [26]. This graft material's main disadvantage is its poor mechanical strength [25]. Resorbable 3D printed $\beta$-TCP scaffolds show potential for bone regeneration [27–29], though 3D printing intricate

**Table 1.** Targeted mechanical properties of human trabecular mandibular bone for scaffold development with matched biomechanical characteristics.

| Characteristics | Trabecular mandibular bone |
|---|---|
| Density (g cm$^{-3}$) | 0.85–1.53; mean 1.14 [38]<br>Edentulous mandible: mean 0.55 [39] |
| Elastic modulus (MPa) | With cortical plates present: 24.9–240.0; mean 96.2 without cortical plates present: 3.5–125.6; mean 56.0 [38] |
| Young's modulus (MPa) | 6.9–199.5 [40] |
| Ultimate compressive strength (MPa) | 0.22–10.44; mean 3.9 [38] |
| Porosity | For trabecular bone (tibia): 50%–90% [41] |

architecture remains challenging due to their brittle nature [30]. Combining TCP with PLA can enhance 3D printability and mechanical properties [31, 32]. Advanced techniques such as Arburg plastic-free forming, similar to injection molding, have emerged to overcome the traditional challenges of 3D printing. With this technique, it is possible to use two materials with different process temperatures simultaneously, allowing the use of a water-soluble support material to create complex geometries and anatomical shapes [33–35]. It is essential to consider material and process compatibility with medical requirements to ensure safe and effective use of 3D printed materials in clinical settings. Neglecting practical considerations such as process requirements, toxicity, adherence to hospital sterilization protocols, and associated side effects can compromise the safety and efficacy of the final product, hindering clinical translation. Therefore, it is recommended that researchers address these issues early in the development phase [36, 37].

In the scope of this study, our objective was to develop a biomimetic 3D printed scaffold specifically designed to effectively address intricate defects in the CMF area. Building upon the insights highlighted earlier, our focus extended toward the crucial aspect of potential clinical translation. The key objective of our research was the fabrication of a scaffold meticulously designed to align with the intricate biomechanical properties of the mandibular bone, as outlined in table 1. This entailed a thorough consideration of design, fabrication, and processing parameters, all aimed at achieving optimal anatomical and biological compatibility. We aim to enhance the scaffold's efficacy in promoting bone regeneration and optimize clinical translatability. We hypothesize that 3D-printed poly(L-lactide-co-D,L-lactide) (PLDLLA) and $\beta$-TCP gyroid scaffolds will possess tunable mechanical properties suitable for CMF applications. Additionally, multiphasic coating strategies using PDA and HAP will enable customization of the scaffolds' surface properties, such as cell adhesion, promoting specific cellular responses, and inhibiting undesirable cell growth as needed. This adaptability makes the constructs promising candidates for various bone regeneration applications.

## 2. Results

### 2.1. CAD part analysis

The analysis results (figure 1, detailed in table S1 in the supplementary data) indicate that the morphological deviation of the additively manufactured scaffolds from the CAD model remains within the expected tolerance for all four models, each designed with specific (WTs, in mm) and porosities (P, in %). The average signed distance between the scanned and CAD models is less than 0.1 mm for all models, with the RMS deviation below 0.13 mm, except for the top surface of WT0.8P70 (0.1886 mm) and the front surface of WT1P60 (0.1749 mm).

For the front surface, the average deviation from the CAD model is 0.0155 mm, with an RMS deviation of 0.1284 mm and a standard deviation of 0.1039 mm. For the top surface, the average deviation is 0.0358 mm, with an RMS deviation of 0.1339 mm and a standard deviation of 0.1288 mm.

Overall, the findings suggest a minor disparity between the CAD model and the scanned gyroid structures, remaining below the 3D printer's drop size threshold (0.2 mm). The top surface exhibits slightly more variation than the front surface.

### 2.2. Mechanical properties

The mechanical properties of the 3D-printed scaffolds were evaluated by analyzing elastic modulus, yield strength, and ultimate compressive strength across different WT and porosities. As shown in figure 2 and detailed in table S2 and figure S1, increasing porosity led to a reduction in elastic modulus. For example, scaffolds with a 1.0 mm WT exhibited a 31.82 MPa decrease in mean elastic modulus when porosity increased from 60% to 70%. A similar trend was observed for yield strength and ultimate compressive strength.

Scaffold geometry played a dominant role in mechanical performance, explaining 87.19% of the variance in mean compressive strength, while build direction contributed 6.76% ($p < 0.0001$). Similarly, geometry accounted for 80.13% of the variance in yield strength, while build direction explained 13.81%. For elastic modulus, geometry contributed

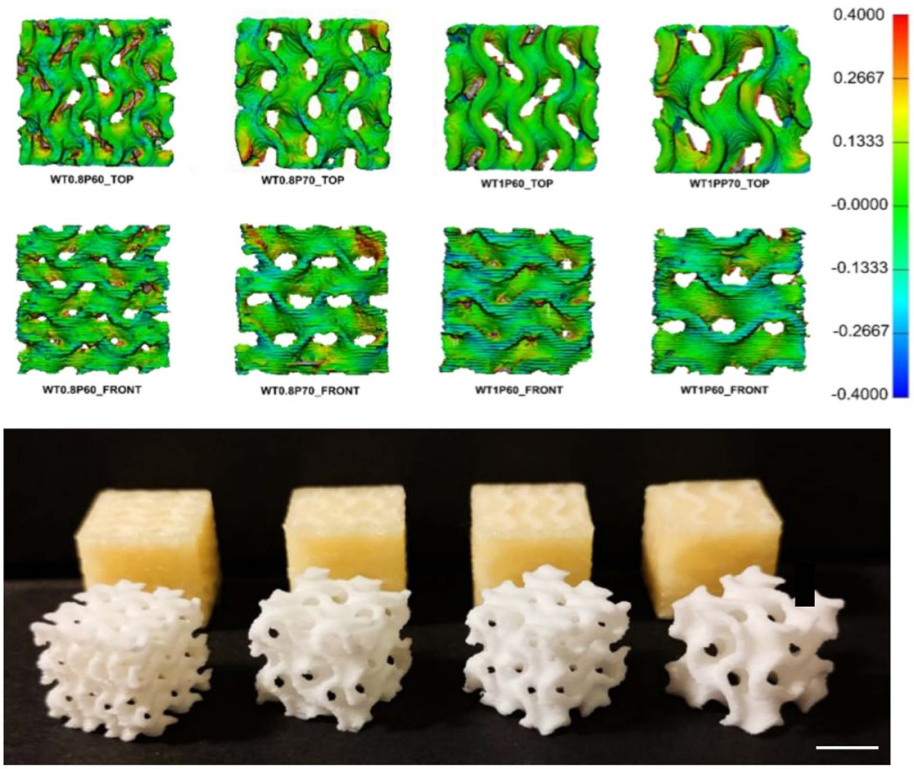


**Figure 1.** Structural and morphological analysis of 3D-printed scaffolds. Top: color-coded surface deviation maps of the top and front surfaces compare the 3D-printed scaffolds to their CAD models. Deviations (in mm) are shown as red (protrusions), blue (recessed areas), and green (close to CAD model). Most deviations fall within the acceptable tolerance of ±0.1333 mm, demonstrating high morphological fidelity. Bottom: Photograph of 3D-printed scaffolds before (background) and after (foreground) support structure removal, arranged by variations in wall thickness (WT, in mm) and porosity (P in %), from left to right: WT0.8P60, WT0.8P70, WT1P60, and WT1P70. Scale bar indicates 5 mm.

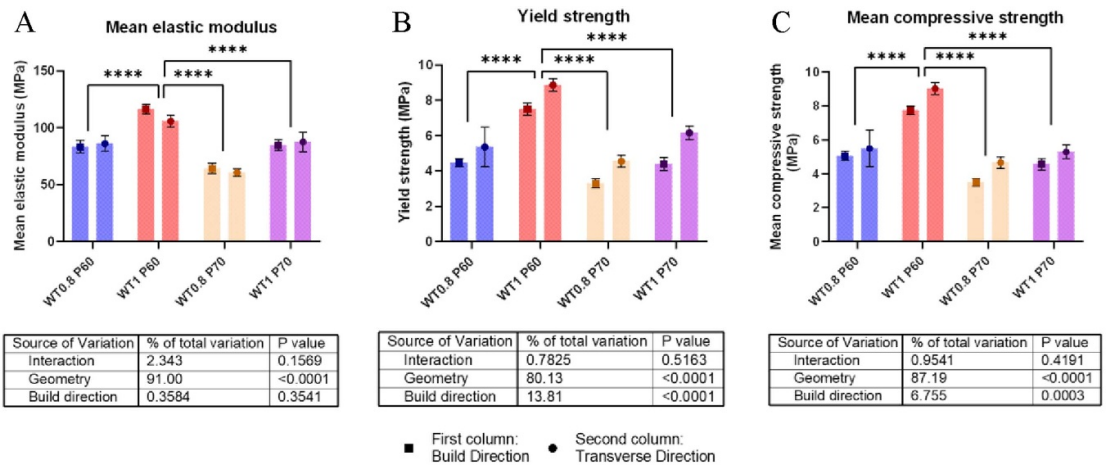


| Source of Variation | % of total variation | P value |
|---|---|---|
| Interaction | 2.343 | 0.1569 |
| Geometry | 91.00 | <0.0001 |
| Build direction | 0.3584 | 0.3541 |

| Source of Variation | % of total variation | P value |
|---|---|---|
| Interaction | 0.7825 | 0.5163 |
| Geometry | 80.13 | <0.0001 |
| Build direction | 13.81 | <0.0001 |

| Source of Variation | % of total variation | P value |
|---|---|---|
| Interaction | 0.9541 | 0.4191 |
| Geometry | 87.19 | <0.0001 |
| Build direction | 6.755 | 0.0003 |

**Figure 2.** Influence of geometry and build direction on the mechanical properties of 3D-printed gyroid scaffolds. Mechanical testing results for three replicates of each scaffold geometry (WT0.8P60, WT0.8P70, WT1P60, and WT1P70) under two testing directions: build direction (■, first column) and transverse direction (●, second column). Data are presented for three mechanical properties: (A) mean elastic modulus (MPa), (B) yield strength (MPa), and (C) mean compressive strength (MPa). Tables below each plot summarize the analysis of variance, detailing the percentage of total variation attributed to geometry, build direction, and their interaction, along with corresponding *p*-values.

92.28%, with build direction having an insignificant effect (0.36%). The lack of interaction between these factors suggests that the effect of build direction remains consistent across different scaffold geometries.

Scaffolds with 1.0 mm WT exhibited superior mechanical properties compared to 0.8 mm WT. The WT1P60 scaffold demonstrated the highest overall performance, with an elastic modulus of 116.43 MPa (build direction) and 105.87 MPa

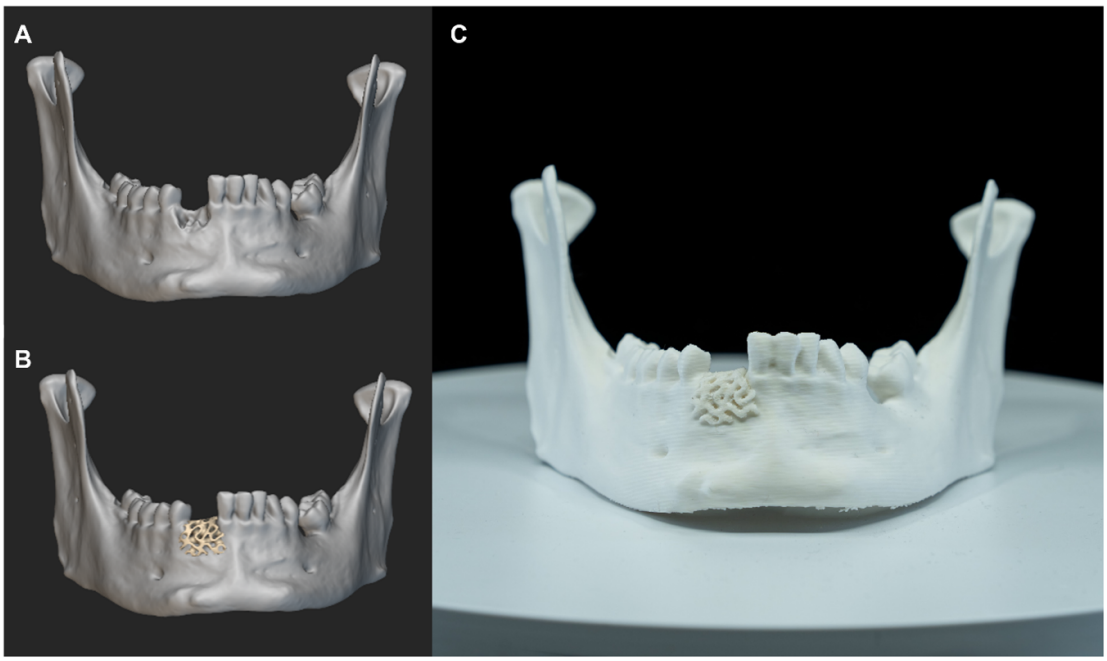


**Figure 3.** Design and fabrication of a patient-specific scaffold for an alveolar bone defect of the mandible. (A): CAD rendering illustrating the alveolar bone defect (B): and the corresponding scaffold placement. (C): 3D-printed anatomical scaffold made from PLDLLA-$\beta$-TCP designed to fit the alveolar bone defect.

(transverse direction), a yield strength of 7.50 MPa and 8.87 MPa, and an ultimate compressive strength of 7.74 MPa and 9.03 MPa, respectively.

These findings highlight the ability to tune porosity and WT to achieve tailored mechanical properties. The WT1P60 scaffold consistently outperformed other designs, closely matching the mechanical properties of human mandibular bone and was selected for all subsequent experiments. (Table 1).

EDX analysis (table S3) confirmed the expected elemental composition of the scaffolds, with carbon (47–51 wt%) and oxygen (36–39 wt%) as the primary constituents, alongside smaller amounts of phosphorus and calcium (5–7 wt%). No significant differences were observed between unprinted, printed, sterilized, or unsterilized samples.

### 2.3. Complex 3D printing of gyroid architecture on mandibular defect

A defect was artificially created on a jaw model, and the scaffold was then 3D printed with PLDLLA-$\beta$-TCP using the same method described in Methods, section 3D printing. After support removal and handling, the anatomically shaped scaffold maintained structural integrity and showed no visible fracture or delamination and no permanent deformation or warping). When seated into the 3D-printed defect model, it showed no observable rocking and remained in place under gentle manual loading; due to the anatomical geometry, only one reproducible seating orientation was possible. Fit was assessed by visual inspection.

The results (figure 3) demonstrate the possibility of printing complex, anatomically shaped structures due to the use of water-soluble support material. The printed scaffold, although having complex angles, proved stable and fitting after being placed in the area of the artificial defect in a fit assessment with the defect model.

### 2.4. Cytotoxicity testing using BJ-1 cells

The qualitative evaluation of the 24 h elution test (ISO 10993-5) (figure 4, top) revealed no morphological changes indicative of cell lysis or cytotoxicity. No signs of cytotoxic product leaching were observed in the test material, while the positive control exhibited clear cytotoxic effects. The quantitative assessment (figure 4, bottom) based on metabolic activity measured via the CellTiter-Blue Cell Viability Assay, showed no significant differences compared to the negative control, with a mean activity of 97.52%. The positive control exhibited markedly reduced activity at 7.19%. For printed disks, mean metabolic activity levels were 102.3% (without support material) and 101.7% (with support material), while the eluate from the porous scaffold showed an activity of 100.8%. The unprinted material controls exhibited levels of 96.25% (unsterilized) and 95.02% (sterilized).

All tested samples exhibited metabolic activities above the 70% non-cytotoxicity threshold, as defined by ISO 10993-5.

Direct cell seeding onto material samples resulted in limited adhesion after 24 h (figure 5, top) and

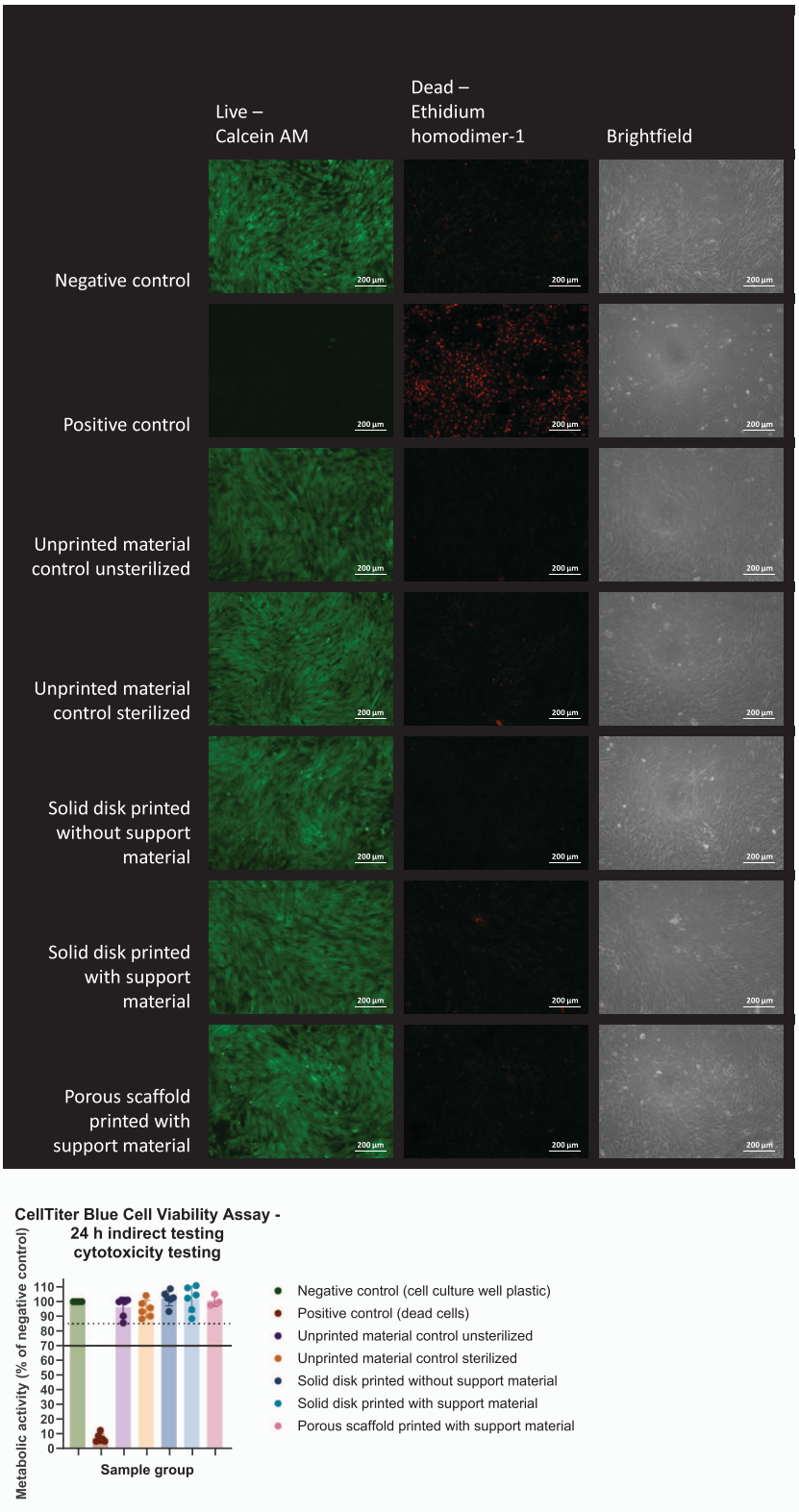


**Figure 4.** Evaluation of cell viability using 24 h indirect qualitative and quantitative cytotoxicity testing using BJ-1 cells (ISO 10993-5). Top: fluorescence images of Calcein AM (green, live cells) and ethidium homodimer-1 (red, dead cells) staining. Bottom: CellTiter-Blue Cell Viability Assay after 24 h exposure to scaffold eluates. Cell metabolic activity is expressed relative to the negative control. The solid line marks the 70% non-cytotoxicity threshold, and the dotted line indicates the 90% target threshold.

72 h (figure S2, top). SEM imaging showed sparse cell adhesion, with no confluency achieved. Quantitative analysis confirmed low metabolic activity (figure 5, bottom and figure S2, bottom). Preincubation of the materials in medium for 24 h improved adhesion, with the solid disk printed with support material performing slightly better than other samples. Metabolic activity remained low in uncoated samples.

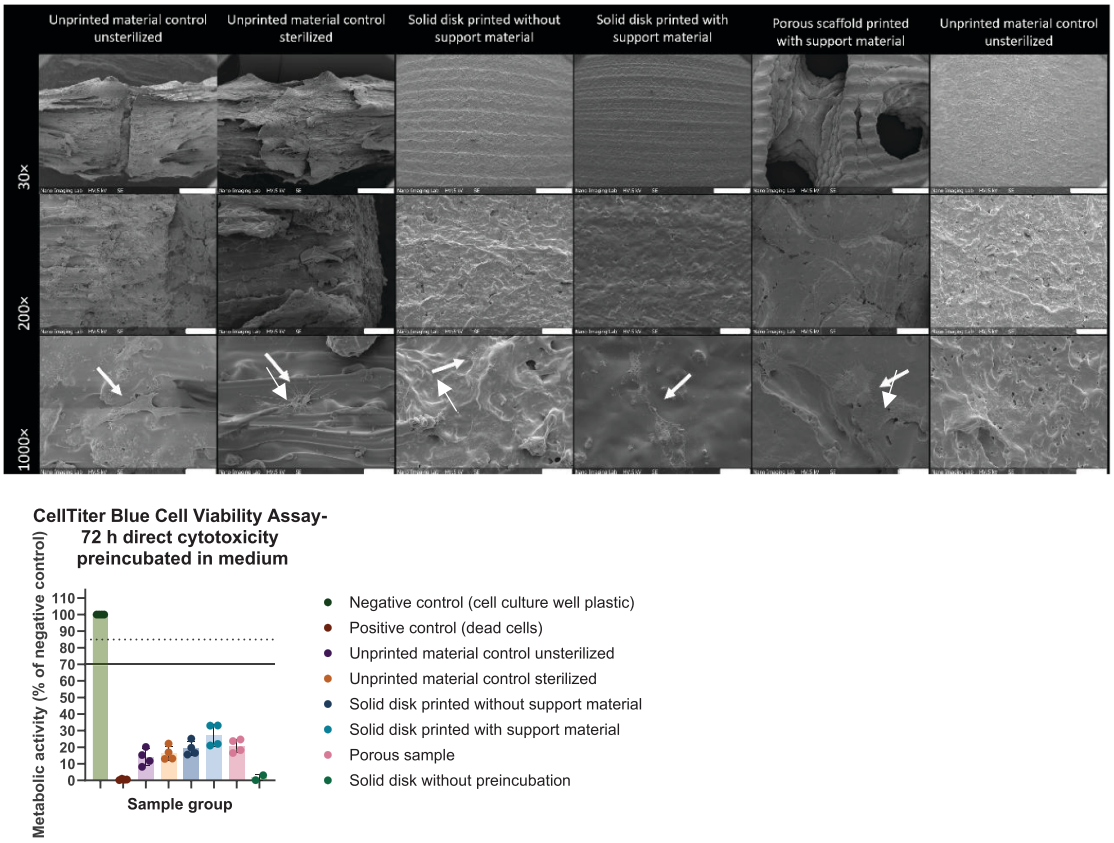


**Figure 5.** Evaluation of BJ-1 cell adhesion after 72 h direct cytotoxicity qualitative and quantitative testing (ISO 10993-5). Top: scanning electron microscopy (SEM) images at 30×, 200×, and 1000× magnifications, showing cell adhesion and morphology on scaffold surfaces. Sample conditions: negative control (cell culture well plastic), positive control (50 µl dimethyl sulfoxide (DMSO)), unprinted material control (sterilized/unsterilized), printed solid disk (with/without support material), porous scaffold (with support material), and solid disk control (without preincubation). Arrows highlight cells adherent to the scaffold surface. Scale bars in the lower right corner in white indicating for upper, middle and lower row 800, 100 and 20 µm. Bottom: CellTiter-Blue Cell Viability Assay quantifying metabolic activity of adherent cells after 72 h exposure to scaffold surfaces. All samples, except the solid disk without preincubation, were preincubated in medium for 24 h. Metabolic activity is expressed relative to the negative control, with the solid line marking the 70% threshold for acceptable metabolic activity (ISO 10993-5).

### 2.5 Coatings

Coating the samples with polydopamine (PDA) or polydopamine hydroxyapatite (PDA–HAP) improved metabolic activity of BJ-1 cells (figures 6, 7 and S3). The coating with PDA only increased the metabolic activity two-fold compared to the uncoated sample. When coating with PDA and HAP, the activity improved further to 5.3-fold. Since metabolic activity is closely associated with cell viability and adhesion, these findings suggest that the synergistic use of PDA and HAP coatings promotes improved cell–material interactions.

Confocal microscopy with live and dead staining was performed after 14 d of BJ-1 cell culture on porous gyroid structures (figure 6). The results showed that the cells on the PDA and PDA–HAP-coated samples proliferated while keeping a physiological morphology; on the contrary, the uncoated samples did not promote any cell adhesion and proliferation. This is consistent with the previous results showing that PDA and PDA–HAP-coatings can significantly improve cell adhesion (see figures 5 and S2).

Surface morphology and cell adhesion trends for different-coatings were further examined via SEM (figure S4), confirming enhanced SaOS-2 cell attachment on PDA-HA-coated samples compared to non-coated and PDA-coated scaffolds.

### 2.6 Osteogenic marker expression and calcium-associated alizarin red S (ARS) staining analysis

The effect of coating with PDA and PDA–HAP was assessed using the osteosarcoma-derived, osteoblast-like cell line SaOS-2 by evaluating the expression of bone-related markers. Confocal imaging revealed differences in cell adhesion behavior and bone matrix protein expression among coatings (figure 8). Interestingly, SaOS-2 cells adhered robustly to uncoated scaffolds, showing expression of mineralization markers bone sialoprotein (IBSP) and Osteocalcin (OCN). PDA-coated and PDA–HAP-coated scaffolds supported moderate cell adhesion, with modest bone matrix protein expression but increased cell coverage and elongation.

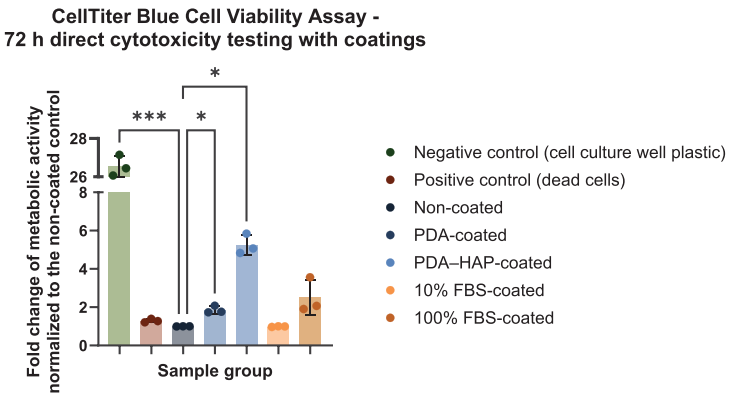


**Figure 6.** CellTiter-Blue Cell Viability Assay quantifying metabolic activity of adherent BJ-1 cells on coated scaffold samples after 72 h of direct cytotoxicity testing. Fold change in cell metabolic activity is presented for various sample groups, normalized to non-coated scaffolds. Additional control groups include preconditioning for 24 h in complete culture medium (DMEM + 10% FBS; labeled '10% FBS') and preconditioning for 24 h in pure serum (100% FBS) as protein-adsorption reference conditions, demonstrating significantly enhanced cell adhesion on polydopamine (PDA)-coated scaffolds, and polydopamine-hydroxyapatite (PDA–HAP)-coated scaffolds compared to the non-coated control.

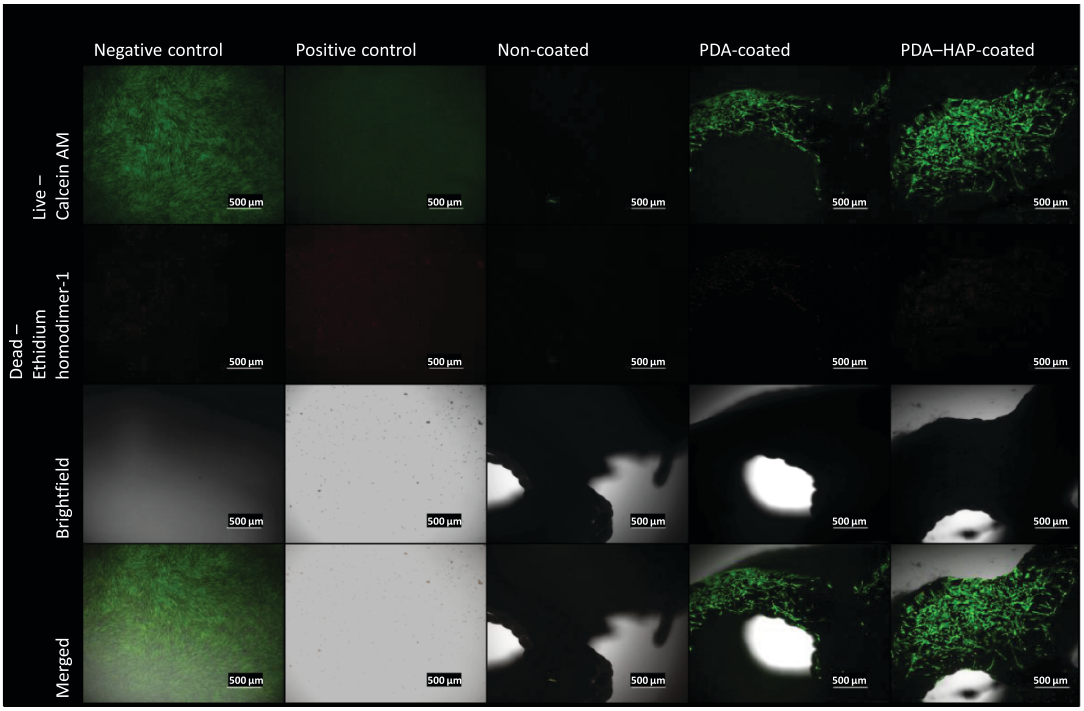


**Figure 7.** Confocal microscopy of qualitative, representative live/dead staining of BJ-1 cells after 14 d of culture on porous gyroid scaffolds. Live cells, negative control as reference, are stained with Calcein-AM (green), and dead cells, positive control as reference, are stained with ethidium homodimer-1(red). Polydopamine (PDA)-coated scaffolds, and polydopamine-hydroxyapatite (PDA–HAP)-coated scaffolds show significant cell proliferation and attachment, with cells maintaining physiological morphology. In contrast, non-coated scaffolds do not support significant cell adhesion or proliferation. The scale bar indicates 500 µm.

The mineralization potential of non-coated, PDA-coated, and PDA–HAP-coated scaffolds was assessed via qualitative and quantitative ARS staining after 10 d in basal medium, with and without SaOS-2 cells. Scaffolds seeded with SaOS-2 cells exhibited notable differences in calcium deposition (figure 9). PDA–HAP-coated scaffolds showed the most intense and uniform calcium-associated ARS staining, whereas non-coated and PDA-coated scaffolds cultured with cells had lighter, patchy staining, suggesting lower calcium deposition. The non-cultured native control displayed minimal staining.

Quantitative analysis (figure 9, Right) showed PDA–HAP-coated scaffolds with cells had the highest absorbance values, while non-coated and PDA-coated scaffolds exhibited lower values.

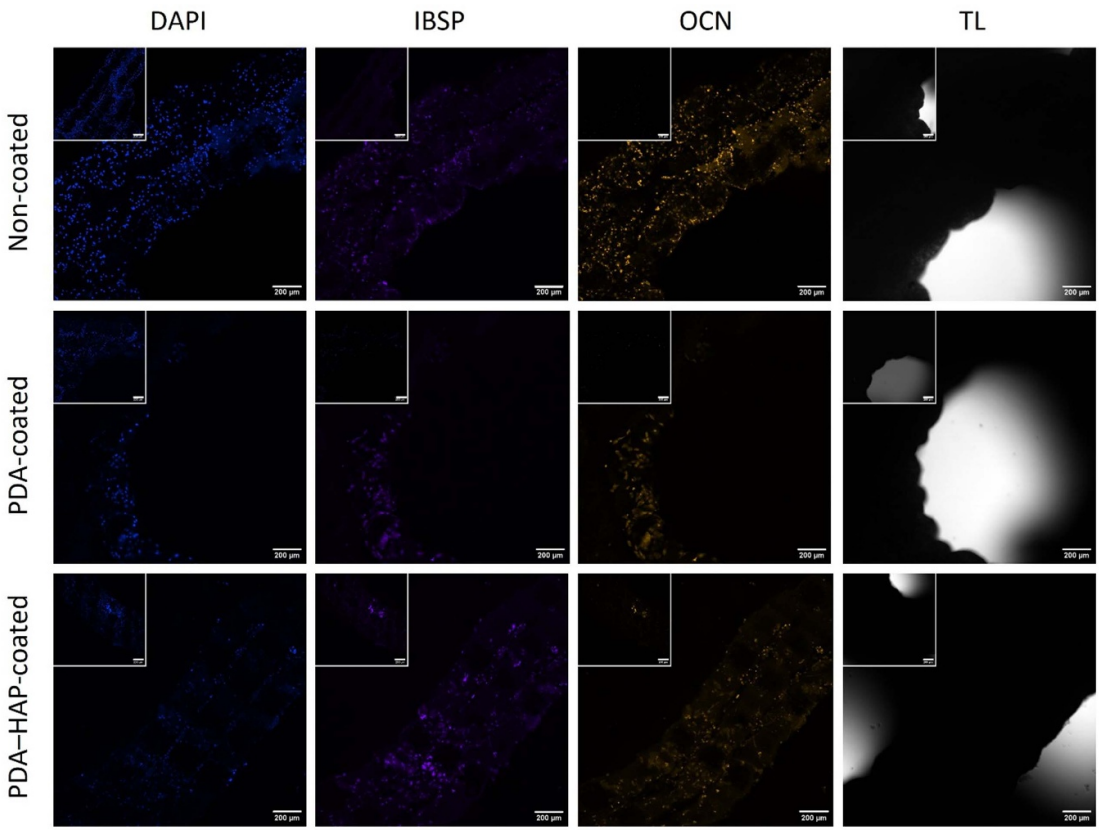


**Figure 8.** Confocal imaging of SaOS-2 cells on coated scaffolds. Confocal microscopy images of SaOS-2 cells cultured for 10 d in basal medium on non-coated, polydopamine (PDA)-coated, and polydopamine-hydroxyapatite (PDA–HAP)-coated scaffolds. Staining: DAPI (nuclei, blue), IBSP (bone sialoprotein, purple), OCN (Osteocalcin, yellow), and transmitted light (TL, bright-field) for scaffold visualization. Images are at 200× magnification ; inserts show secondary antibody staining only. Scale bars: 200 μm (main images and insets). SaOS-2 cells adhered to all scaffolds but exhibited higher metabolic activity uncoated scaffolds.

## 3. Discussion

The present study investigated the mechanical properties and biocompatibility of 3D-printed gyroid constructs for CMF applications. The findings revealed promising insights, indicating that these scaffolds are both biocompatible and mechanically suitable, making them attractive candidates for future clinical applications in treating craniofacial bone defects. Furthermore, the study highlighted the potential of functionalizing HAP with PDA to significantly enhance cell adhesion.

### 3.1. CAD analysis

In CMF applications, precise anatomical fit is crucial for optimal functionality and aesthetic restoration [42]. Surface scanning validated the accuracy of the 3D-printed gyroid scaffolds with deviations within a 0.2 mm tolerance. While the RMS values suggest overall acceptability, the dispersion shown by the standard deviation points to notable surface variations. Overall, the CAD-to-scan comparison indicates high geometric fidelity of the printed scaffolds at the assessed surfaces, with deviations remaining within the predefined tolerance. The observed dispersion (standard deviation) reflects local surface variability on the complex TPMS geometry and scanner accessibility, rather than providing a direct measure of internal architecture. In contrast to conventional linear-patterned scaffolds [21, 43], this study introduces a biomimetic gyroid architecture, offering improved design capabilities. A limitation of the present work is that internal pore and pore-throat size distributions and quantitative interconnectivity metrics were not evaluated using volumetric methods (e.g. micro-CT-based pore network analysis).

### 3.2. Mechanical properties

Given the considerable variation in size and complexity of CMF defects, the ability to customize scaffold mechanical properties is essential to meet diverse patient needs [10]. The mechanical analysis revealed that porosity and WT significantly influenced the elastic modulus, yield strength, and ultimate compressive strength of the scaffolds. Notably, all tested designs fall within the reported ranges for mandibular bone properties [38], with the WT1P60 pattern demonstrating the most favorable performance. The elastic modulus of WT1P60 aligns well with that of mandibular bone (24.9–240 MPa), an important criterion for mimicking natural bone stiffness and maintaining biomechanical function

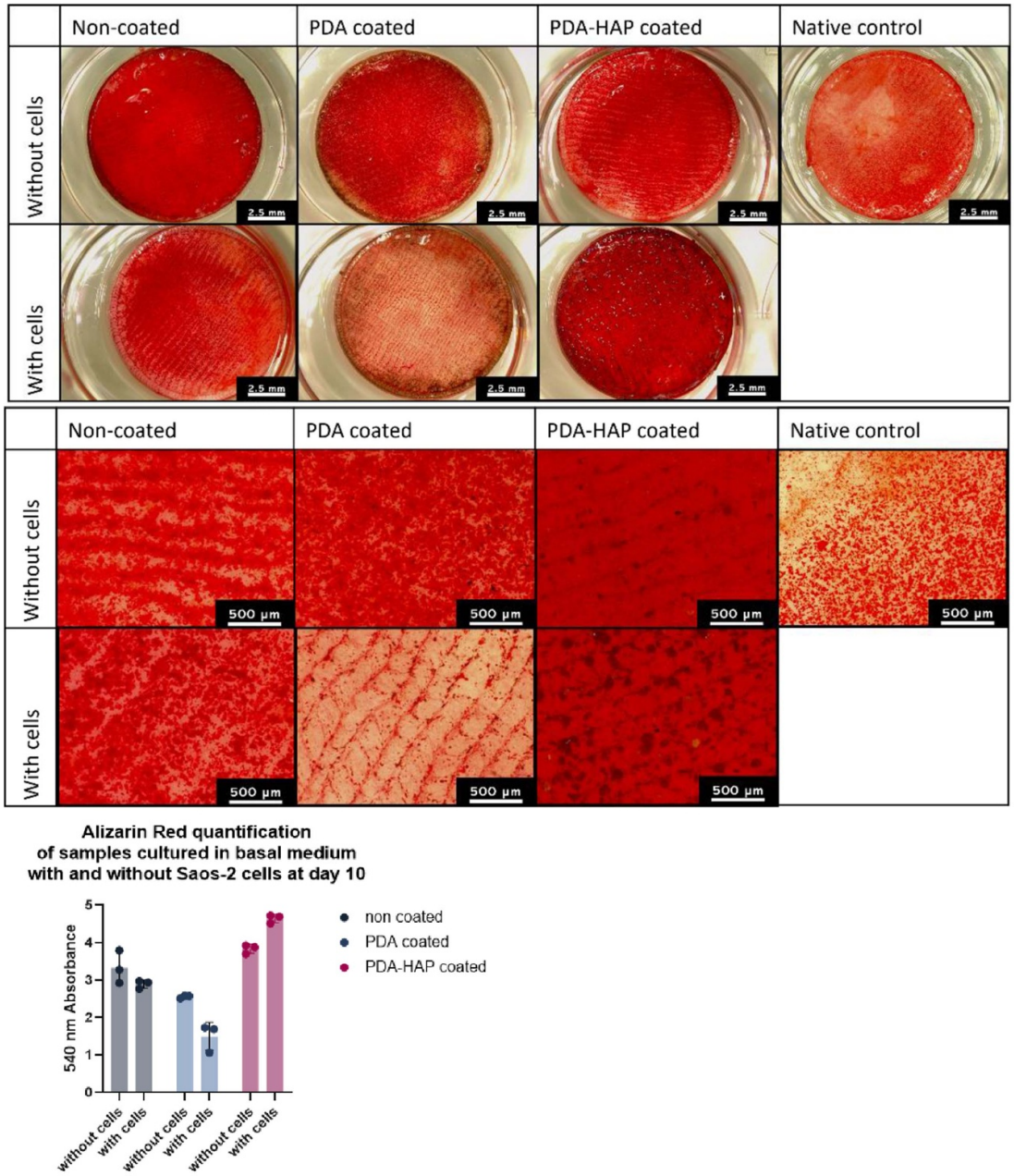


**Figure 9.** Alizarin red staining of samples cultured for 10 d in basal medium. Top: Macroscopic images (50× magnification) showing calcium deposition on non-coated, PDA-coated, and PDA–HAP-coated scaffolds, with and without SaOS-2 cells. The control was a sample that was not cultured in basal medium. Middle: microscopic images (380× magnification) providing detailed views of staining patterns. Non-coated and PDA-coated scaffolds with cells exhibit lighter, irregular staining, indicating lower calcium deposition. PDA–HAP-coated scaffolds with cells show dense, uniform staining. The control exhibits staining, confirming the presence of calcium in the material. Bottom: quantitative analysis of alizarin red S staining. The control served as a blank. PDA–HAP-coated scaffolds exhibited the highest calcium deposition.

*in vivo* [38]. Furthermore, the yield strength and ultimate compressive strength of the WT1P60 scaffold closely match those of mandibular bone, ensuring that the scaffold can withstand similar physiological loads. The scaffold's yield strength, reaching up to 8.87 MPa, and its compressive strength of 9.03 MPa, fall within the upper range of values reported for trabecular mandibular bone. This indicates the scaffold's ability to maintain structural integrity under mechanical stress, further supporting its potential use in load-bearing applications such as mandibular reconstruction. The stress–strain curves display a non-linear stage, attributed to manufacturing irregularities, surface abnormalities, and sample settlement until achieving complete contact with the testing machine's crosshead surface. This behavior is consistent with previous findings in porous scaffold testing [44, 45] and akin to ductile polymers.

The Young's modulus showed a slight difference between samples compressed in the build and transverse directions, indicating anisotropic mechanical

behavior. This anisotropy likely results from the layer-by-layer deposition process in AM, which enhances bonding within horizontal layers but may lead to weaker interlayer adhesion. Structural imperfections such as gaps or delamination can further reduce mechanical performance in the transverse (vertical) direction, where poor layer bonding creates weak points that compromise scaffold strength [46].

This anisotropy is characteristic of natural bone and may be intentionally designed to emulate the mechanical profile of trabecular bone for regenerative purposes [39, 47]. The study revealed that the WT1P60 scaffold exhibits a higher apparent Young's modulus under uniaxial compression in the build and transverse direction compared to the other designs, suggesting that it might be potentially tuned for designing a shape-specific bone graft. In agreement with earlier findings [48], as expected increased porosity was associated with decreased yield strength and compressive strength. Importantly, the elastic modulus and compressive strength values measured in both the build and transverse directions were consistent with those reported for human mandibular trabecular bone, reinforcing the scaffold's suitability for multi-directional mechanical loading regardless of implant orientation.

### 3.3. Complex 3D printing of patient-specific gyroid architecture for mandibular defect

The integration of water-soluble support material into gyroid constructs eliminates shape limitations, allowing for the fabrication of geometries suited to intricate craniofacial defects within the constraints of the printer's build chamber (154 × 134 × 230 mm). This volume is sufficient to accommodate the printing of an entire human mandible, and in practice, enables the simultaneous production of multiple scaffolds. This capability supports the production of highly customized, patient-specific scaffolds. The results demonstrate the feasibility of printing complex gyroid structures, offering a clear advantage over traditional rectilinear patterns in adapting to diverse anatomical sites. Despite the complexity of their geometries, the printed scaffolds exhibited structural stability and conformed accurately to the artificial defect during a fit assessment using a 3D-printed mandible model. These findings highlight the clinical viability and mechanical reliability of this approach for addressing complex facial bone defects.

### 3.4. Cytotoxicity & coating

CMF defects often occur in sensitive and critical anatomical regions, in close proximity to vital nerves and vascular structures of the head. Therefore, ensuring the absence of cytotoxic byproducts and confirming appropriate biocompatibility are essential prerequisites for successful clinical translation. Accordingly, the *in vitro* biological assessment was intentionally designed as a preliminary evaluation using established cell models to investigate cytocompatibility, adhesion, and mineralization under controlled conditions. While these models cannot fully reproduce the complexity of the *in vivo* bone environment, they provide essential insight into material–cell interactions and represent a necessary step prior to more comprehensive biological investigations.

Consistent with this rationale, subsequent cell viability assays performed using post-processed and sterilized samples exposed to 24 h material extracts demonstrated no detectable cytotoxic effects *in vitro*, as assessed with the BJ-1 human fibroblast cell line in accordance with ISO 10993-5 (Biological evaluation of medical devices). These findings indicate that the manufacturing workflow including the use of water-soluble support materials and the applied sterilization procedures does not adversely affect the biological safety of the final construct and supports its cytocompatibility.

The reduced viability observed when cells were directly seeded on the materials can be attributed to limited adhesion to uncoated materials, as samples pre-treated with 10% FBS showed a significant improvement in adhesion compared to the uncoated control group, where cells failed to adhere. Additionally, scaffolds printed with support structures showed slightly improved performance, possibly due to increased surface roughness following support removal. Nevertheless, overall cell adhesion to the material remained notably low, which is consistent with expectations for hydrophobic materials [17]. Although Fairag *et al* demonstrated that 3D printed scaffolds without surface modifications may be suitable as bone substitutes for defects, the current findings highlight the superior cell adhesion properties of PDA and PDA–HAP-coated samples [49]. For tissue regeneration purposes, our material needs to be coated to overcome hydrophobic properties and allow for cell adhesion, as shown by pre-treatment with 10% FBS. Since FBS is not clinically translatable and is subject to donor variability, a standardized PDA–HAP coating, previously studied by this group, was applied to enhance hydrophilicity, promote adhesion, enable biomolecule immobilization, and support clinical translation by leveraging a compound already used in medical contexts [21, 50].

The benefit of coating was confirmed via confocal microscopy, which revealed confluent cellular layers without evident changes in cell morphology on PDA and PDA–HAP coated samples compared to single-celled states on uncoated counterparts.

Recent studies have demonstrated that PDA-coatings enhance the osteogenic differentiation of bone marrow-derived mesenchymal stromal cells on implant surfaces, both *in vitro* and *in vivo*, accelerating bone formation and improving osseointegration [51, 52]. Additionally, significant bone regeneration was reported in a mouse calvaria defect model with

Poly(L-lactide) (PLLA) with a similar PDA-adenosine coating [53]. These findings demonstrate the versatile bioactivity of PDA, particularly its capacity to immobilize biomolecules and boost the scaffold's therapeutic potential.

The unexpected lower calcium-associated ARS staining observed in the polydopamine (PDA)-coated scaffolds may be attributed to the effects of dopamine on the osteosarcoma-derived osteoblast-like SaOS-2 cell line. While PDA typically enhances cell adhesion and scaffold bioactivity [21, 50], recent findings from Sun *et al* reported that PDA can activate the dopamine receptor DRD1 and modulate cell behavior via the cAMP/PKA pathway, affecting RhoA activity and cytoskeletal organization. In addition, Gao *et al* demonstrated that DRD1 is expressed in in OS732 osteosarcoma cells and that DRD1 activation reduces proliferation, which was associated with decreased ERK1/2 and PI3K/Akt signaling [54, 55]. We therefore hypothesize that DRD1-mediated signaling may also affect the osteosarcoma-derived SaOS-2 cell line used here [55], reducing the number of viable matrix-producing cells and thereby contributing to the lower mineral deposition observed in the PDA coated group. In contrast, the PDA-HAP coated scaffolds may mitigate this effect by providing osteoconductive mineral cues and may partially mask PDA exposed functional groups, supporting cell attachment and osteogenic activity, promoting mineralization [4, 12]. Calcium-associated ARS staining was assessed after 10 d in basal medium in samples with and without SaOS-2 cells. Because the scaffold contains $\beta$-TCP (and PDA–HAP includes a calcium phosphate phase), ARS staining reflects both scaffold-derived calcium/background and any cell-associated deposition. Therefore, ARS is reported here as a comparative, non-specific readout, and conclusions regarding cell-mediated mineralization are limited; orthogonal methods (e.g. SEM/EDX) are required to confirm mineral deposition.

The tunability of scaffolds coated with PDA and PDA–HAP extends further through localized functionalization, enabling precise customization for specific therapeutic purposes. PDA-coatings can be strategically applied near resection margins to exploit their photothermal and anti-tumor properties for localized cancer control and recurrence prevention. Simultaneously, PDA–HAP-coatings can be focused on regions requiring bone regeneration, supporting mineralization and tissue integration. This spatial approach enhances overall scaffold performance and bridges the gap between oncological and regenerative applications, offering a multifunctional solution for complex clinical challenges.

This study employed large pore sizes based on prior research indicating benefits for mesenchymal stem cell proliferation on PLA scaffolds [56, 57]. However, further justification and optimization of pore architecture are necessary to suit specific anatomical requirements. While the present work focused on material properties and biocompatibility, future studies should evaluate scaffold design in the context of site-specific mechanical and regenerative demands. In addition, 3D printing could be combined with cell-laden hydrogel bioinks for direct cell delivery [58].

Although PDA functionalization significantly improves cell adhesion, it remains experimental and is not currently approved for medical devices. Dopamine is a clinically available drug that can be administered parenterally to treat cases of pronounced hypotension and shock [59, 60] and cannot cross the brain–blood barrier [61]. The use of a clinically approved molecule enhances the potential for regulatory compliance and facilitates clinical translation, offering a more streamlined alternative to the approval process required for new compounds.

While the base material is available in medical grade form and similar coatings have been previously validated *in vivo* [43, 62], preclinical studies are essential to confirm this scaffolds performance and clinical suitability. A thorough understanding of the biological interactions and long term behavior of the scaffold within host tissue will require extensive *in vivo* testing [63]. In addition, the scaffold's longevity and degradation profile must be assessed to ensure reliable performance over time in the intended physiological environment.

### 3.5. Novelty

Literature supports the use of PLA/$\beta$-TCP composite scaffolds for bone regeneration applications [64, 65]. In parallel, TPMS architectures such as gyroid, diamond, and primitive have been increasingly explored because they offer continuous surfaces, high interconnectivity, and tunable mechanical behavior [66]. Many prior TPMS studies focus on neat PLA or other polymers without a ceramic phase [62, 67], whereas PLA or PLDDLA and $\beta$-TCP composites are more commonly reported in strut-based lattices or non-TPMS porous designs [68, 69]. Surface bioactivation is often achieved using direct calcium phosphate deposition, bioactive glass coatings, or biologic functionalization, while here we use PDA as a versatile interfacial platform combined with HAP to introduce mineral cues [70, 71]. Importantly, the PDA approach can be adapted to immobilize or nucleate other functional coatings beyond HAP, enabling flexible tailoring of the surface to the intended application. Finally, we incorporate a clinically relevant sterilization route using hydrogen peroxide plasma, strengthening translational feasibility compared with *in vitro* sterilization routines such as ethanol baths and UV exposure [67]. Overall, in comparison to prior reports that remain at the level of generic test geometries, we demonstrate manufacturing of a patient specific scaffold for an alveolar bone defect as a clinically relevant use case.

## 4. Conclusion

This study highlights the possibility of AM for creating complex structures to address CMF defects. It shows that the mechanical properties of 3D printed gyroid architectures can be effectively controlled by adjusting porosity and WT. Among the tested designs, the WT1P60 pattern with a WT of 1 mm and a porosity of 60% emerged as a strong candidate for mandibular bone regeneration, offering an elastic modulus and compressive strength within the desired range. Throughout the entire process, from 3D printing to sterilization, the PLDDLA-$\beta$-TCP material maintained its integrity, and the printed scaffolds exhibited no cytotoxic effects. However, a functionalization step using PDA and HAP was required to enable effective cell adhesion.

Overall, these findings support the development of patient-specific 3D-printed composite scaffolds that combine mechanically relevant TPMS architectures with a bioactive, adaptable mineral interface as a surgical innovation manufactured at the point-of-care.

## 5. Materials & methods

### 5.1. Gyroid structure for morphological and mechanical analysis

All CAD models were created using nTopology software (Version 3, nTopology, New York, USA). The initial scaffolds were designed based on the gyroid unit cell, defined by the following equation:

To construct each scaffold, the gyroid unit cells were arranged in a tessellated pattern within a rectangular volume box (figure 10). The dimensions of this volume box were: length ($l$) = 10.0 mm, width ($w$) = 10.0 mm, and height ($h$) = 10.0 mm.

To achieve target porosities (P) ranging from approximately 60% to 70%, the size of the gyroid unit cell was systematically adjusted. The WT was optimized at either 0.8 mm or 1.0 mm, depending on the porosity level. Table 2 provides detailed parameters of the gyroid scaffolds. Pore architecture is defined at the CAD level by the implicit gyroid TPMS design. In contrast to strut-based lattices, the gyroid TPMS yields a continuous pore phase, i.e. an interconnected pore network by design. In this work, the characteristic architectural length scale is therefore governed by the gyroid unit cell size and WT (table 2), which were selected to achieve the designed porosities. Imaging-based quantification of internal pore size/throat diameter distributions (e.g. micro-CT) was not performed in this study; instead, manufacturing fidelity to the CAD model was assessed via surface scanning (CAD part analysis).

The support structures were generated separately by extruding the designed system perpendicular to the build plate. The lattice support structure was formed by inverting the corresponding gyroid geometry of the bounding box, ensuring structural stability while maintaining an offset of 0.0001 mm from the scaffold.

### 5.2. 3D design—samples for biological analysis

To accommodate the 24-well plate featuring 12 mm diameter wells, porous disks and discoid lattice structures based on the WT1P60 pattern were designed. The creation process for these structures closely paralleled that of the original gyroid scaffolds. To maintain consistency, the height of the porous disk was standardized at 1.5 mm, and the height of the solid disk was adjusted to match the material volume of the porous design. Support structures for the discoid lattice structure and the control group 'disk with support structure' were again fashioned using perpendicular extrusion and inversion techniques.

### 5.3. Design of complex scaffold with gyroid architecture for mandibular defect

To showcase the capability of producing intricate structures for clinical applications, a STL file of a mandible, sourced from a prior publication, was utilized [72]. An artificial alveolar defect was generated digitally in Geomagic Freeform Plus (v. 2019, 3D Systems, Rock Hill, USA) by mirroring the healthy contralateral anatomy onto the defect side, virtually reducing the dental crowns to the alveolar bone level, and subtracting the mirrored anatomy to create a defect/augmentation volume STL. Thin edges ($<$1 mm) were smoothed to avoid fragile features, and the defect volume was offset by $+$0.2 mm to facilitate insertion. The design process then followed the established workflow for gyroid structures in nTopology, as previously described. However, in this instance, the imported STL of the designed augmentation volume was selected as an implicit body instead of a conventional box, allowing for a more tailored and complex scaffold design.

### 5.4. 3D printing

The designs and support structures'STL files were brought into the Arburg Slicer software (Arburg GmbH + Co KG, Lossburg, Germany) and compiled into an AFJ file. Bioresorbable composite granules RESOMER LR 706 S $\beta$-TCP from the RESOMER BIORESORBABLE POLYMERS FOR MEDICAL DEVICES portfolio (Evonik Industries AG, Essen, Germany) were obtained as a pre-mixed, medical-grade product, containing 70% poly(L-lactide-co-D, L-lactide) with a 70:30 ratio and 30% $\beta$-tricalcium phosphate (PLDDLA-$\beta$-TCP) [31, 73]. The material is manufactured in compliance with IPEC-GMP guidelines and ISO 13485 standards, ensuring its suitability for implantable medical devices. The granules are manufactured through a compounding process that ensures the homogeneous distribution of $\beta$-TCP within the polymer matrix, eliminating the

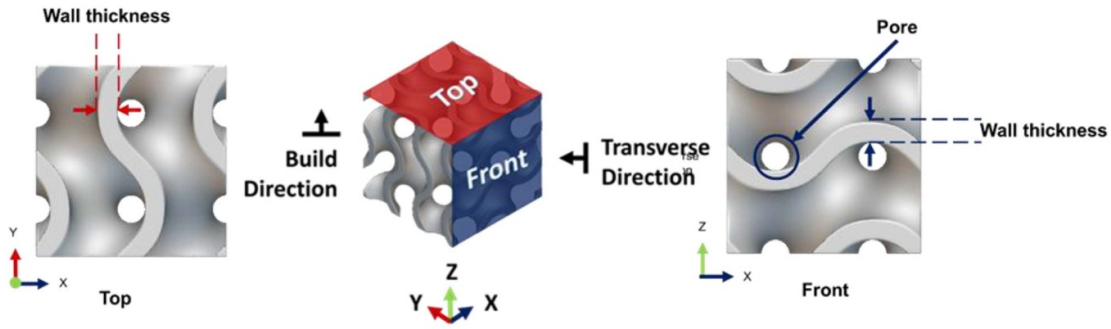


**Figure 10.** Characteristics of the gyroid scaffold structure, illustrating the defined top and front surfaces, wall thickness, and pore architecture. The build direction is represented along the *Z*-axis, with the transverse direction shown for reference.

**Table 2.** Design parameters of gyroid scaffolds.

| Assigned name | Wall thickness (mm) | Unit cell size ($mm^2$) | Designed porosity (%) |
|---|---|---|---|
| WT0.8P60 | 0.8 | 3.9 | 60.29 |
| WT1P60 | 1 | 4.87 | 60.4 |
| WT0.8P70 | 0.8 | 5.2 | 69.59 |
| WT1P70 | 1 | 6.5 | 70.46 |

need for any additional blending or preparation in our laboratory. The composite granules' density, Young's modulus, and fracture strain were 1.24 g $mm^{-3}$, 3500–4500 MPa, and <10% for injection molded specimens [73]. ARMAT 11 (Arburg GmbH + Co KG Lossburg, Germany), a water-soluble polyvinyl alcohol-based material, was used for support structures. All samples were 3D printed with the Arburg freeformer 200-3X (Arburg GmbH + Co KG, Lossburg, Germany) using the temperature specifications from the material providers. The mandible model was fabricated using fused filament fabrication with the BambuLab X1 Carbon printer (BAMBULAB LIMITED, Shenzhen, China). The chosen printing material was polylactic acid (PLA Matte Bambu Filament, BAMBULAB LIMITED).

### 5.5. Post-processing & sterilization

The 3D printed support structures were removed by immersing the parts in tap water within an ultrasonic bath for 90 min, with water refreshed between each 30 min interval. The samples were then air dried at room temperature. They were packed in sterilization peel-pouches (Steriking, Wipak Medical, Finland). Sterilization at 55 °C using hydrogen peroxide plasma with the Steris Vpro (Steris, Basingstoke, UK) for 19 min, following internal hospital sterilization protocols, was chosen due to its superiority over ultraviolet and steam sterilization for porous polymeric composite scaffolds [74], ensuring thorough penetration of the gyroid structures, while minimizing thermal damage.

### 5.6. CAD part analysis

To assess the superficial printing accuracy, three replicates of each design were scanned using an intraoral scanner (3Shape TRIOS, Copenhagen, Denmark). Subsequently, the printed models were compared to the initial design and evaluated for accuracy using the 3D software Materialise 3-matic 17.0 (Materialise, Leuven, Belgium). The morphological deviation of the 3D printed scaffolds from the CAD model was evaluated by comparing the scanned scaffold surfaces to the respective CAD model values for designed surfaces. RMS values were used to quantify the difference between the physical scaffolds and the digital models. The RMS value was compared to a ±0.4 mm threshold to determine whether the differences between the scanned and CAD models were within acceptable tolerance. The results of the analysis were visually represented as color maps. All triangles below the histogram's minimum threshold value were colored blue, and all those above were colored red. Surface differences between ±0.4 mm were represented by the color bar, which was interpolated from turquoise to green to orange between the minimum and maximum threshold values. A green color overlay showed an excellent model agreement.

### 5.7. Mechanical characterization

To conduct mechanical characterization of the scaffolds and assess the impact of variations in WT and porosity levels, each of the four designs outlined in table 2 was subjected to testing using three replicates. The scaffolds were compressed between rigid metal plates using a uniaxial compression setup on an Instron 3344 machine with a maximum load capacity of 200 kN. Before testing, the gyroid scaffolds were conditioned in distilled water at 37 °C for 1–4 h following ISO 13781:1991 guidelines to assess their performance when wet. Compression tests were conducted under displacement-controlled conditions at

a rate of 1 mm $min^{-1}$, following the general principles of ISO 604:2002 and adapted for the porous, additively manufactured scaffolds to capture both elastic behavior and progressive structural collapse. Scaffold anisotropy was assessed by testing along and perpendicular to the printing direction to account for layer-dependent mechanical behavior inherent to additively manufactured structures. This approach reflects clinically relevant mandibular loading, where load transfer from mastication may act along different scaffold axes depending on defect geometry and implantation orientation. Compression was stopped at a maximum strain 15%. This upper limit was chosen to exceed mechanical failure and capture post-failure deformation and collapse behavior. The compressive modulus ($Ec$) was determined by measuring the maximum slope of the elastic region in the stress–strain curve. The elastic modulus was calculated using the formula: $Ec = \sigma/\varepsilon = F \times A \times \Delta L/L$, where $\sigma$ is stress, $F$ is the vertical reaction force, $A$ is the initial solid cross-sectional area of the scaffold, $\varepsilon$ is strain, $\Delta L$ is the displacement of the upper surface, and $L$ is the initial length of the scaffold. Force and displacement data were used to generate stress–strain curves, considering the sample's height and cross-sectional area. Young's modulus was determined through linear regression analysis of the elastic zone. Compressive yield strength was calculated at the point of deviation from linearity, and the ultimate compressive strength was the maximum stress before the scaffold layer collapsed.

### 5.8. Coating & surface modification

The surface functionalization of RESOMER LR 706 S $\beta$-TCP disks and gyroid scaffolds, henceforth referred to as samples, was carried out using polydopamine (PDA) and nano-hydroxyapatite (HAP) based on our previously published protocol from Chi *et al*, 2022 [21] (see figure S3). The samples were first immersed in a freshly prepared dopamine solution (2 mg $ml^{-1}$ in 10 mM Tris buffer, pH 8.5). To promote the formation of a thin, adherent PDA layer on the surface, the samples were placed on an orbital shaker at 24 rpm and 25 °C for 24 h. Throughout the coating process, the solution was gently agitated to ensure even coating and to prevent aggregation of self-polymerizing PDA nanoparticles.

After PDA deposition, the samples were rinsed three times with sterile Milli-Q water to remove any residual dopamine and air-dried at room temperature, avoiding oven drying to preserve the material's integrity. These samples, now referred to as PDA-coated, were then subjected to further functionalization.

The immobilization of nano-HAP was performed by immersing the PDA-coated samples in an HAP solution (50 mg $ml^{-1}$). The samples were incubated on the orbital shaker under the same conditions (24 rpm, 25 °C) for 7 d. Following this incubation, the samples were washed three times with sterile Milli-Q water and air-dried at room temperature. These fully functionalized samples are referred to as PDA–HAP coated in this study, while uncoated RESOMER LR 706 S $\beta$-TCP samples were used as the control group.

### 5.9. Biological characterization

#### *5.9.1. Cell culture and seeding*

Cell lines of BJ1 fibroblasts for the initial indirect cytotoxicity and adhesion tests, and osteoblast-like SaOS-2 cells for the mineralization tests were cultured and expanded in basal (DMEM, Thermo Fisher, Zürich, Switzerland) supplemented with 10% FBS (Corning, Glendale, AZ, USA) and 1% penicillin/streptomycin (P/S, Roche Diagnostics GmbH, Rotkreuz, Switzerland) at 37 °C, 5% $CO_2$, and 95%–98% rH. The medium was replaced every two days.

#### *5.9.2. Indirect cytotoxicity and adhesion test*

Indirect cytotoxicity testing was performed according to ISO 10993:5. Material extracts were obtained by incubating the samples for 24 h at 37 °C in 500 µl DMEM/10% FBS/1% P/S per sample, according to ISO 10993:12. BJ1 cells were seeded in 24-well cell culture plates (TPP, Trasadingen, Switzerland) at a density of approximately $1 \times 10^5$ cells $cm^{-2}$ (20,000 cells per well) and incubated in a humidified incubator at 37 °C and 5% $CO_2$. After 24 h, the medium was exchanged for sample conditioned extracts. As a positive control for cytotoxicity, 50 µl DMSO was added to the cell culture medium. The cell culture well served as a negative control, allowing for optimal culturing conditions. The tested groups included unprinted material controls, both unsterilized and sterilized granules, solid disks printed with and without support material, and porous gyroid scaffolds (WT1P60 pattern) printed with support material as defined in our design specification under '3D design—samples for biological analysis'. After another 24 h, the qualitative and quantitative cytotoxicity measurements were performed. To evaluate the adhesion potential, according to the direct cytotoxicity test according to ISO 10993:5, the BJ-1 cell suspension was directly added to the samples at the same density and cultured for 24 and 72 h before analysis. Again, the negative control was cell culture well plastic, and the positive control was 50 µl DMSO. The tested samples included unprinted material controls, both sterilized and unsterilized, solid disks printed with and without support material, and porous scaffolds printed with support material. An additional control included a solid disk that was not preincubated in medium for 24 h.

Direct cytotoxicity testing on coated scaffolds after 72 h of cell culture was performed. The samples included non-coated, Polydopamine-coated (PDA), and Polydopamine and Hydroxyapatite-coated (PDA–HAP) samples functionalized according to section 'Coating/ Surface modification'. Additional

controls involved preconditioning for 24 h either in complete culture medium (DMEM + 10% FBS; '10% FBS') or in pure serum (100% FBS) prior to cell seeding. The negative control remained cell culture well plastic, and the positive control was 50 µl DMSO.

*5.9.3. Cytotoxicity testing via Promega CellTiter-Blue Cell Viability Assay*

CellTiter Blue reagent (CellTiter-Blue Cell Viability Assay, Promega Corporation, Madison, WI, USA) was added to the cell culture medium and incubated for four hours. The absorbance was measured at 570 nm using a microplate reader (Synergy H1, BioTek Instruments, Winooski, VT, USA). The percentage of cell viability was calculated as follows: Cell viability % $= (A_{\text{sample}} - A_{\text{blank}})/(A_{\text{CRL-}} - A_{\text{blank}}) \times 100$. All experiments were run with three replicate samples and repeated multiple times. Each data point in the figure represents the mean of three replicates.

*5.9.4. Live/dead staining*

The samples were washed twice with phosphate-buffered saline (PBS) and then incubated with Invitrogen™ LIVE/DEAD™ Cell Imaging Kit (Thermo Fisher, Zürich, Switzerland) for 30 min according to the manufacturer's protocol. The samples were visualized using an EVOS FL AUTO 2 imaging system (Thermo Fisher, Zürich, Switzerland) for 24 and 72 h qualitative viability testing and the confocal microscope Eclipse Ti2 (Nikon, Amstelveen, The Netherlands) for different coatings after 10 d in culture with basal medium, both with and without BJ-1 cells. The coatings analyzed included non-coated, PDA-coated, and PDA–HAP-coated samples. Three biological replicates were analyzed in separate technical triplicates.

*5.9.5. SEM*

7. SEM was performed to evaluate adhesion of BJ-1 cells to the different surfaces and surface treatments

After washing with PBS twice, the samples were fixed in 10% formalin for 20 min. For SEM, the samples were washed with Milli-Q water and then dehydrated in a graded ethanol series. When critical-point dried, they were sputter-coated with gold. The micro morphologies and chemical compositions of the scaffolds were investigated using (SEM, Phillips XL30, Eindhoven, Netherlands) with EDX. The samples for cell adhesion after 24 and 72 h were sputtered with gold and observed at an accelerating voltage of 5 kV at different magnifications.

EDX analysis was conducted at an accelerating voltage of 10 kV. For EDX, we prepared the following groups unprinted and unsterilized material controls, consisting of the raw granules, unprinted and sterilized material controls, with the raw granules subjected to our in-house plasma sterilization protocol, 3D-printed disks without support material, and 3D-printed disks with support material.

*5.9.6. Immunofluorescence*

Confocal imaging of non-coated, PDA-coated, and PDA–HAP-coated scaffolds seeded with SaOS-2 cells was conducted after 10 d of culture in basal medium. Briefly, samples were washed twice with PBS, permeabilized with 0.1% Triton X-100 for 15 min at room temperature with shaking, and subsequently blocked with 1.6% BSA in PBS for 1 h under the same conditions.

Primary antibodies were prepared following the manufacturer's instructions, and samples were incubated overnight with 5 µg ml$^{-1}$ IBSP (bone sialoprotein, Invitrogen, Rockford, IL, USA) and 10 µg ml$^{-1}$ OCN (Osteocalcin, R&D Systems, Minneapolis, MN, USA). After washing three times with PBS, secondary antibodies; 1.5 µg ml$^{-1}$ Alexa Fluor™ 546 Goat anti-Mouse IgG1 for Osteocalcin and 4 µg ml$^{-1}$ Alexa Fluor™ 488 Goat anti-Rabbit IgG for bone sialoprotein (both Invitrogen, Rockford, IL, USA)—were applied and incubated at 37 °C for 1 h. Following incubation, samples were washed three times with PBS and counterstained with 1 µg ml$^{-1}$ DAPI (Biotium, Fremont, CA) for nuclear visualization, followed by three additional PBS washes. Imaging was performed using an EVOS FL AUTO 2 imaging system (Thermo Fisher, Zürich, Switzerland) and an Eclipse Ti2 confocal microscope (Nikon, Amstelveen, The Netherlands).

*5.9.7. ARS staining*

Disks were cultured for 10 d in basal medium with and without SaOS-2 cells. Following the incubation period, samples were rinsed with PBS and fixed in 10% formalin for 15 min. After fixation, the scaffolds were stained with 2% ARS solution (pH 4.2) for 30 min at room temperature. Excess stain was removed by washing the samples thoroughly with distilled water. Macroscopic images were captured at 50× magnification, while microscopic images were obtained at 380× magnification to evaluate calcium deposition visually using a Leica DVM6a digital microscope (Leica Microsystems, Wetzlar, Germany). The scaffolds included non-coated, PDA-coated, and PDA–HAP-coated samples, both with and without SaOS-2 cells. Control groups comprised unseeded scaffolds (without cells) and native scaffolds not subjected to culture.

After qualitative imaging, the ARS stain was eluted using 10% cetylpyridinium chloride in 10 mM sodium phosphate buffer (pH 7.0) for 30 min. The absorbance of the eluted stain was measured at 540 nm using a spectrophotometer to quantify the amount of calcium deposited in the scaffolds. Absorbance values were normalized to the blank.

### 5.10. Statistical analysis

The data was collected and organized using Microsoft Excel from Microsoft 365 MSO (Microsoft Cooperation, Redmond, WA, USA). Descriptive statistics such as normality testing, mean, standard deviation, and ANOVA were conducted using GraphPad Prism 10.1.0 (GraphPad Software, Inc., La Jolla, CA, USA). Statistical significance was set at a $p$-value less than 0.05, denoted by an asterisk. Significance levels for $p$-values are indicated by asterisks as follows: one asterisk (*) for $p \leqslant 0.05$, two asterisks (**) for $p \leqslant 0.01$, three asterisks (***) for $p \leqslant 0.001$, and four asterisks (****) for $p < 0.0001$. A two-way ANOVA factoring in geometry and build direction was performed for mechanical analysis and Sidak's multiple comparisons tests. For cytotoxicity testing, a mixed effects analysis matching biological replicates was served with a Dunnet's multiple comparison test compared to the uncoated controls.

## Acknowledgment

The authors would like to thank Nadja Rohr and Sabrina Karlin, Biomaterials and Technology, University Center for Dental Medicine Basel, for the support with SEM analysis. We acknowledge the collaborative effort and support of Neha Sharma (Swiss MAM RG) who contributed to the design and conceptualization of the scaffolds. We want to thank laboratory technician Cecilia Bärtschi, for her valuable support. Furthermore, we acknowledge the contribution of the students Isabella Ortiz Drada and Anna Griselin.

Registered trademarks, trade names, and proprietary names are used in this content. Even if not specifically marked as such, all relevant trademark protections and regulations apply.

## Data availability statement

All data that support the findings of this study are included within the article (and any supplementary files).

Supplementary Data available at https://doi.org/10.1088/1748-605X/ae55ed/data1.

## Funding

This work was funded by the Innovation Focus Regenerative Surgery of the University Hospital Basel and by the Werner Siemens Foundation through the Minimally Invasive Robot-Assisted Computer-guided LaserosteotomE II (MIRACLEII) project. Additionally, it was financially supported by AO CMF (project: AOCMF-21-04S). AO CMF is a clinical division of the AO Foundation—an independent medically guided not-for-profit organization.

## Conflict of interest

The authors declare no conflict of interest.

## Ethics statement

All experiments were performed in accordance with relevant institutional guidelines and regulations. This study did not involve human participants or animal subjects. Only *in vitro* cell-line based assays were conducted, and no ethical approval was required.

## Author contributions

Céline Tourbier 0000-0002-2809-4067
Conceptualization (equal), Data curation (equal), Formal analysis (equal), Investigation (equal), Methodology (equal), Visualization (equal), Writing – original draft (equal), Writing – review & editing (equal)

Valentina Basoli 0000-0002-4703-7308
Conceptualization (equal), Formal analysis (equal), Funding acquisition (equal), Methodology (equal), Supervision (equal), Writing – review & editing (equal)

Michaela Maintz 0000-0003-4502-3655
Data curation (equal), Investigation (equal), Methodology (equal), Writing – review & editing (equal)

Elena Della Bella 0000-0001-5151-7390
Investigation (equal), Methodology (equal), Supervision (equal), Writing – review & editing (equal)

Martin James Stoddart 0000-0002-9538-1517
Resources (equal), Writing – review & editing (equal)

Florian M Thieringer 0000-0003-3035-9308
Resources (equal), Writing – review & editing (equal)

## References

[1] Roseti L, Parisi V, Petretta M, Cavallo C, Desando G, Bartolotti I and Grigolo B 2017 Scaffolds for bone tissue engineering: state of the art and new perspectives *Mater. Sci. Eng. C.* **78** 1246–62

[2] Nyberg E L, Farris A L, Hung B P, Dias M, Garcia J R, Dorafshar A H and Grayson W L 2017 3D-printing technologies for craniofacial rehabilitation, reconstruction, and regeneration *Ann. Biomed. Eng.* **45** 45–57

[3] Hollister S J 2005 Porous scaffold design for tissue engineering *Nat. Mater.* **4** 518–24
[4] Bose S, Vahabzadeh S and Bandyopadhyay A 2013 Bone tissue engineering using 3D printing *Mater. Today* **16** 496–504
[5] Entezari A, Roohani I, Li G, Dunstan C R, Rognon P, Li Q, Jiang X and Zreiqat H 2019 Architectural design of 3D printed scaffolds controls the volume and functionality of newly formed bone *Adv. Healthc. Mater.* **8** 1801353
[6] Ma W, Lu H, Xiao Y and Wu C 2025 Advancing organoid development with 3D bioprinting *Organoid Res.* **1** 025040004
[7] McWilliam R H, Chang W, Liu Z, Wang J, Han F, Black R A, Wu J, Luo X, Li B and Shu W 2023 Three-dimensional biofabrication of nanosecond laser micromachined nanofibre meshes for tissue engineered scaffolds *Biomater. Transl.* **4** 104–14
[8] 2023 Video of first patient at the USB receiving 3D-printed implant from in-house production (available at: https://dbe.unibas.ch/en/news/details-408/video-of-first-patient-at-the-usb-to-receive-3d-printed-implant-from-in-house-production/) (Accessed 14 February 2024)
[9] Sharma N, Zubizarreta-Oteiza J, Tourbier C and Thieringer F M 2023 Can steam sterilization affect the accuracy of point-of-care 3D printed polyetheretherketone (PEEK) customized cranial implants? An investigative analysis *J. Clin. Med.* **12** 2495
[10] Honigmann P, Sharma N, Okolo B, Popp U, Msallem B and Thieringer F M 2018 Patient-specific surgical implants made of 3D printed PEEK: material, technology, and scope of surgical application *BioMed. Res. Int.* **2018** 4520636
[11] Ying J, Yu H, Cheng L, Li J, Wu B, Song L, Yi P, Wang H, Liu L and Zhao D 2023 Research progress and clinical translation of three-dimensional printed porous tantalum in orthopaedics *Biomater. Transl.* **4** 166–79
[12] Bose S, Roy M and Bandyopadhyay A 2012 Recent advances in bone tissue engineering scaffolds *Trends Biotechnol.* **30** 546–54
[13] Zhang Q *et al* 2022 High-strength hydroxyapatite scaffolds with minimal surface macrostructures for load-bearing bone regeneration *Adv. Funct. Mater.* **32** 2204182
[14] Schoen A H 1970 Infinite periodic minimal surfaces without self-intersections *Report* No.: C–98 (available at: https://ntrs.nasa.gov/citations/19700020472) (Accessed 9 August 2023)
[15] Spece H, DeSantis P M and Kurtz S M 2022 Development of an architecture-property model for triply periodic minimal surface structures and validation using material extrusion additive manufacturing with polyetheretherketone (PEEK) *J. Mech. Behav. Biomed. Mater.* **133** 105345
[16] Yang Y *et al* 2022 Gaussian curvature–driven direction of cell fate toward osteogenesis with triply periodic minimal surface scaffolds *Proc. Natl Acad. Sci. USA.* **119** e2206684119
[17] Vacaras S *et al* 2019 Understanding the basis of medical use of poly-lactide-based resorbable polymers and composites—a review of the clinical and metabolic impact *Drug Metab. Rev.* **51** 570–88
[18] Farah S, Anderson D G and Langer R 2016 Physical and mechanical properties of PLA, and their functions in widespread applications—a comprehensive review *Adv. Drug Deliv. Rev.* **107** 367–92
[19] Yan Q, Dong H, Su J, Han J, Song B, Wei Q and Shi Y 2018 A review of 3D printing technology for medical applications *Engineering* **4** 729–42
[20] Karanth D, Song K, Martin M L, Meyer D R, Dolce C, Huang Y and Holliday L S 2023 Towards resorbable 3D-printed scaffolds for craniofacial bone regeneration *Orthod. Craniofac. Res.* **26** 188–95
[21] Chi M, Li N, Cui J, Karlin S, Rohr N, Sharma N and Thieringer F M 2022 Biomimetic, mussel-inspired surface modification of 3D-printed biodegradable polylactic acid scaffolds with nano-hydroxyapatite for bone tissue engineering *Front. Bioeng. Biotechnol.* **10** 989729
[22] Cui J, Ma C, Li Z, Wu L, Wei W, Chen M, Peng B and Deng Z 2016 Polydopamine-functionalized polymer particles as templates for mineralization of hydroxyapatite: biomimetic and *in vitro* bioactivity *RSC Adv.* **6** 6747–55
[23] Wang Y-C, Dai H-L, Li Z-H, Meng Z-Y, Xiao Y and Zhao Z 2021 Mesoporous polydopamine-coated hydroxyapatite nano-composites for ROS-triggered nitric oxide-enhanced photothermal therapy of osteosarcoma *J. Mater. Chem. B* **9** 7401–8
[24] Su T *et al* 2022 Adhesion-enhancing coating embedded with osteogenesis-promoting PDA/HA nanoparticles for peri-implant soft tissue sealing and osseointegration *Bio-Des Manuf.* **5** 233–48
[25] Roca-Millan E, Jané-Salas E, Marí-Roig A, Jiménez-Guerra Á, Ortiz-García I, Velasco-Ortega E, López-López J and Monsalve-Guil L 2022 The application of beta-tricalcium phosphate in implant dentistry: a systematic evaluation of clinical studies *Materials* **15** 655
[26] Bohner M, Santoni B L G and Döbelin N 2020 β-tricalcium phosphate for bone substitution: synthesis and properties *Acta Biomater.* **113** 23–41
[27] Russmueller G *et al* 2015 Tricalcium phosphate-based biocomposites for mandibular bone regeneration—a histological study in sheep *J. Craniomaxillofac. Surg.* **43** 696–704
[28] Tarafder S, Balla V K, Davies N M, Bandyopadhyay A and Bose S 2013 Microwave-sintered 3D printed tricalcium phosphate scaffolds for bone tissue engineering *J. Tissue Eng. Regen. Med.* **7** 631–41
[29] Pihlman H, Keränen P, Paakinaho K, Linden J, Hannula M, Manninen I-K, Hyttinen J, Manninen M and Laitinen-Vapaavuori O 2018 Novel osteoconductive β-tricalcium phosphate/poly(L-lactide-co-e-caprolactone) scaffold for bone regeneration: a study in a rabbit calvarial defect *J. Mater. Sci.: Mater. Med.* **29** 156
[30] Hwa L C, Rajoo S, Noor A M, Ahmad N and Uday M B 2017 Recent advances in 3D printing of porous ceramics: a review *Curr. Opin. Solid State Mater. Sci.* **21** 323–47
[31] RESOMER® bioresorbable polymers for medical devices (available at: https://healthcare.evonik.com/en/medical-devices/bioresorbable-polymers/standard-polymers) (Accessed 20 June 2023)
[32] Elhattab K, Bhaduri S B and Sikder P 2022 Influence of fused deposition modelling nozzle temperature on the rheology and mechanical properties of 3D printed β-tricalcium phosphate (TCP)/polylactic acid (PLA) composite *Polymers* **14** 1222
[33] Bayart M, Dubus M, Charlon S, Kerdjoudj H, Baleine N, Benali S, Raquez J-M and Soulestin J 2022 Pellet-based fused filament fabrication (FFF)-derived process for the development of polylactic acid/hydroxyapatite scaffolds dedicated to bone regeneration *Materials* **15** 5615
[34] Charlon S and Soulestin J 2020 Thermal and geometry impacts on the structure and mechanical properties of part produced by polymer additive manufacturing *J. Appl. Polym. Sci.* **137** 49038
[35] Ramezani Dana H, Barbe F, Delbreilh L, Azzouna M B, Guillet A and Breteau T 2019 Polymer additive manufacturing of ABS structure: influence of printing direction on mechanical properties *J. Manuf. Processes* **44** 288–98
[36] Culmone C, Smit G and Breedveld P 2019 Additive manufacturing of medical instruments: a state-of-the-art review *Addit. Manuf.* **27** 461–73
[37] Bartnikowski M, Vaquette C and Ivanovski S 2020 Workflow for highly porous resorbable custom 3D printed scaffolds

using medical grade polymer for large volume alveolar bone regeneration *Clin. Oral Implants Res.* **31** 431–41
[38] Misch C E, Qu Z and Bidez M W Mechanical properties of trabecular bone in the human mandible: implications for dental implant treatment planning and surgical placement *J. Oral Maxillofac. Surg.* 1999 **57** 700–6; discussion 706–708
[39] O'Mahony A M, Williams J L, Katz J O and Spencer P 2000 Anisotropic elastic properties of cancellous bone from a human edentulous mandible: elastic properties of cancellous bone from an edentulous mandible *Clin. Oral Implants Res.* **11** 415–21
[40] Lakatos É, Magyar L and Bojtár I 2014 Material properties of the mandibular trabecular bone *J. Med. Eng.* **2014** 470539
[41] Karageorgiou V and Kaplan D 2005 Porosity of 3D biomaterial scaffolds and osteogenesis *Biomaterials* **26** 5474–91
[42] Dewey M J and Harley B A 2021 Biomaterial design strategies to address obstacles in craniomaxillofacial bone repair *RSC Adv.* **11** 17809–27
[43] Sun X *et al* 2023 Polydopamine-coated 3D-printed β-tricalcium phosphate scaffolds to promote the adhesion and osteogenesis of BMSCs for bone-defect repair: mRNA transcriptomic sequencing analysis *J. Mater. Chem. B* **11** 1725–38
[44] Spece H, Yu T, Law A W, Marcolongo M and Kurtz S M 3D printed porous PEEK created via fused filament fabrication for osteoconductive orthopaedic surfaces *J. Mech. Behav. Biomed. Mater.* **109** 103850 2020 Sept 1
[45] Caiazzo F, Alfieri V and Bujazha B D 2021 Additive manufacturing of biomorphic scaffolds for bone tissue engineering *Int. J. Adv. Manuf. Technol.* **113** 2909–23
[46] Herath B, Suresh S, Downing D, Cometta S, Tino R, Castro N J, Leary M, Schmutz B, Wille M-L and Hutmacher D W 2021 Mechanical and geometrical study of 3D printed Voronoi scaffold design for large bone defects *Mater. Des.* **212** 110224
[47] Lu Y, Zhao W, Cui Z, Zhu H and Wu C 2019 The anisotropic elastic behavior of the widely-used triply-periodic minimal surface based scaffolds *J. Mech. Behav. Biomed. Mater.* **99** 56–65
[48] Zaharin H A, Abdul Rani A M, Azam F I, Ginta T L, Sallih N, Ahmad A, Yunus N A and Zulkifli T Z A 2018 Effect of unit cell type and pore size on porosity and mechanical behavior of additively manufactured Ti6Al4V scaffolds *Materials* **11** 2402
[49] Fairag R, Rosenzweig D H, Ramirez-Garcialuna J L, Weber M H and Haglund L 2019 Three-dimensional printed polylactic acid scaffolds promote bone-like matrix deposition *in vitro ACS Appl. Mater. Interfaces* **11** 15306–15
[50] Tolabi H, Bakhtiary N, Sayadi S, Tamaddon M, Ghorbani F, Boccaccini A R and Liu C 2022 A critical review on polydopamine surface-modified scaffolds in musculoskeletal regeneration *Front. Bioeng. Biotechnol.* **10** 1008360
[51] Wang H, Lin C, Zhang X, Lin K, Wang X and Shen S G 2019 Mussel-inspired polydopamine coating: a general strategy to enhance osteogenic differentiation and osseointegration for diverse implants *ACS Appl. Mater. Interfaces* **11** 7615–25
[52] Rim N G, Kim S J, Shin Y M, Jun I, Lim D W, Park J H and Shin H 2012 Mussel-inspired surface modification of poly(L-lactide) electrospun fibers for modulation of osteogenic differentiation of human mesenchymal stem cells *Colloids Surf. B Biointerfaces* **91** 189–97
[53] Ahmad T, Byun H, Lee J, Madhurakat Perikamana S K, Shin Y M, Kim E M and Shin H 2020 Stem cell spheroids incorporating fibers coated with adenosine and polydopamine as a modular building blocks for bone tissue engineering *Biomaterials* **230** 119652
[54] Sun X, Wu C, Tian X, Wang P, Guo J, Shao Z and Wei Q 2024 Activation of dopamine receptor D1 and downstream cellular functions by polydopamine *ACS Biomater. Sci. Eng.* **10** 420–8
[55] Gao J, Zhang C, Gao F and Li H 2017 The effect and mechanism of dopamine D1 receptors on the proliferation of osteosarcoma cells *Mol. Cell. Biochem.* **430** 31–36
[56] Velioglu Z B, Pulat D, Demirbakan B, Ozcan B, Bayrak E and Erisken C 2019 3D-printed poly(lactic acid) scaffolds for trabecular bone repair and regeneration: scaffold and native bone characterization *Connect. Tissue Res.* **60** 274–82
[57] Shi F, Fang X, Zhou T, Huang X, Duan K, Wang J, Qu S, Zhi W and Weng J 2022 Macropore regulation of hydroxyapatite osteoinduction via microfluidic pathway *Int. J. Mol. Sci.* **23** 11459
[58] Chu H, Zhang K, Rao Z, Song P, Lin Z, Zhou J, Yang L, Quan D and Bai Y 2023 Harnessing decellularised extracellular matrix microgels into modular bioinks for extrusion-based bioprinting with good printability and high post-printing cell viability *Biomater. Transl.* **4** 115–27
[59] Russell J A, Gordon A C, Williams M D, Boyd J H, Walley K R and Kissoon N 2021 Vasopressor therapy in the intensive care unit *Semin. Respir. Crit. Care Med.* **42** 59–77
[60] Wang L, Han L, Xue P, Hu X, Wong S-W, Deng M, Tseng H C, Huang B-W and Ko C-C 2021 Dopamine suppresses osteoclast differentiation via cAMP/PKA/CREB pathway *Cell Signal* **78** 109847
[61] Obray J D, Small C A, Baldwin E K, Jang E Y, Lee J G, Yang C H, Yorgason J T and Steffensen S C 2022 Dopamine D2-subtype receptors outside the blood-brain barrier mediate enhancement of mesolimbic dopamine release and conditioned place preference by intravenous dopamine *Front. Cell. Neurosci.* **16** 944243
[62] Brucoli M *et al* 2019 The 'European zygomatic fracture' research project: the epidemiological results from a multicenter European collaboration *J. Craniomaxillofac. Surg.* **47** 616–21
[63] Hatt L P, Thompson K, Helms J A, Stoddart M J and Armiento A R 2022 Clinically relevant preclinical animal models for testing novel cranio-maxillofacial bone 3D-printed biomaterials *Clin. Transl. Med.* **12** e690
[64] Wang B, Ye X, Chen G, Zhang Y, Zeng Z, Liu C, Tan Z and Jie X 2024 Fabrication and properties of PLA/β-TCP scaffolds using liquid crystal display (LCD) photocuring 3D printing for bone tissue engineering *Front. Bioeng. Biotechnol.* **12** 1273541
[65] Wang W, Liu P, Zhang B, Gui X, Pei X, Song P, Yu X, Zhang Z and Zhou C 2023 Fused deposition modeling printed PLA/nano β-TCP composite bone tissue engineering scaffolds for promoting osteogenic induction function *Int. J. Nanomed.* **18** 5815–30
[66] Ma J, Li Y, Mi Y, Gong Q, Zhang P, Meng B, Wang J, Wang J and Fan Y 2024 Novel 3D printed TPMS scaffolds: microstructure, characteristics and applications in bone regeneration *J. Tissue Eng.* **15** 20417314241263689
[67] Thai T H *et al* 2025 3D printed triply periodic minimal surface scaffolds enhanced human exfoliated deciduous teeth stem cell proliferation and differentiation for oral and maxillofacial bone tissue engineering *Polym. Eng. Sci.* **65** 4374–86
[68] Ni X, Feng J, Liang M, Zhou F, Xia Y, Dong Z, Xue Q, Li Z, Pu F and Xia P 2025 Enhancing bone repair with β-TCP-based composite scaffolds: a review of design strategies and biological mechanisms *Orthop. Res. Rev.* **17** 313–40
[69] Sánchez-Cepeda A, Pazos M C, Leonardo P-A, Ingrid S-C, Correa-Araujo L S, María De Lourdes C G and Vera-

Graziano R 2024 Functionalization of 3D printed poly(lactic acid)/graphene oxide/β-tricalcium phosphate (PLA/GO/TCP) scaffolds for bone tissue regeneration application *RSC Adv.* **14** 39804–19

[70] Li Q, Xu Y, Zhang X, Sun M, Xing T, Kang H, Lv C and Wang Y 2025 Polydopamine-modified PCL/β-TCP bioprinting scaffolds for bone regeneration and infection control *ACS Appl. Bio Mater.* **8** 9496–509

[71] Nitschke B M, Beltran F O, Hahn M S and Grunlan M A 2024 Trends in bioactivity: inducing and detecting mineralization of regenerative polymeric scaffolds *J. Mater. Chem. B* **12** 2720–36

[72] Msallem B, Sharma N, Cao S, Halbeisen F S, Zeilhofer H-F and Thieringer F M 2020 Evaluation of the dimensional accuracy of 3D-printed anatomical mandibular models using FFF, SLA, SLS, MJ, and BJ printing technology *J. Clin. Med.* **9** 817

[73] Evonik Nutrition & Care GmbH 2018 Technical data sheet—RESOMER LR 706 S (Evonik Nutrition & Care GmbH) (available at: https://usbch-my.sharepoint.com/personal/celine_tourbier_usb_ch/_layouts/15/onedrive.aspx?id=%2Fpersonal%2Fceline%5Ftourbier%5Fusb%5Fch%2FDocuments%2FProjekte%2FAlveolar%20Mesh%2FEvonik%20information%2FRESOMER%C2%AE%20LR%20706%20S%2FTechnical%20datasheet%20RESOMER%20LR%20706%20S%2Epdf&parent=%2Fpersonal%2Fceline%5Ftourbier%5Fusb%5Fch%2FDocuments%2FProjekte%2FAlveolar%20Mesh%2FEvonik%20information%2FRESOMER%C2%AE%20LR%20706%20S) (Accessed 20 June 2023)

[74] Pérez Davila S, González Rodríguez L, Chiussi S, Serra J and González P 2021 How to sterilize polylactic acid based medical devices? *Polymers* **13** 2115